Direct observation of Li6PS5Cl–NMC electrochemical reactivity in all-solid-state cells

Paul Naillou, Adrien Boulineau, Eric de Vito, Enora Lavanant, Philippe Azaïs

Energy Storage Materials 75 (2025) 104050

Contents lists available at ScienceDirect

Energy Storage Materials

journal homepage: www.elsevier.com/locate/ensm

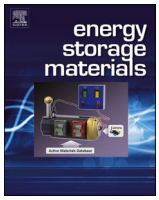

Direct observation of Li_6PS_5Cl–NMC electrochemical reactivity in all-solid-state cells

Paul Naillou [a,*], Adrien Boulineau [a], Eric De Vito [a], Enora Lavanant [b], Philippe Azaïs [a]

[a] Université Grenoble Alpes, CEA, LITEN, Grenoble 38000, France
[b] Umicore Specialty Powders France, 54 avenue Rhin et Danube, Grenoble 38100, France

ARTICLE INFO

Keywords:
Lithium batteries
Solid-state batteries
Sulfide electrolytes
NMC compound
Layered oxides

ABSTRACT

Sulfide solid electrolytes have demonstrated some of the highest known lithium ion conductivities and are expected to participate in the incoming generation of all-solid-state lithium-ion batteries (ASSLIB). Amongst the best promising electrolytes, several lithium thiophosphates have been extensively studied for their outstanding performances. However, they also suffer from their narrow electrochemical stability window, leading to a range of various redox reactions during cycling when used in electrochemical cells. As a result, losses of capacity and increases of cell impedance are systematically observed. As already pointed out, Li_6PS_5Cl argyrodite-type electrolyte undergoes a series of decomposition reactions during cycling, previously investigated by several spectroscopic, electrochemical and DFT studies. However, this work provides a direct high resolution observation of the decomposition products of Li_6PS_5Cl and their spatial distribution in a composite cathode based on Ni-rich NMC compound ($LiNi_xMn_yCo_{1-x-y}O_2$, $x > 0.8$) through scanning/ transmission electron microscopy (S/TEM). This study focuses on the understanding of the oxidative mechanisms and reports the detailed observations of LiCl, Li_3PS_4, P_2S_5, P_2O_5, NiS_x and Li_2O compounds.

1. Introduction

Besides limiting the fire hazard of thermal runaways by removing flammable liquid solvents, ASSLIB open new prospects such as the use of metallic Li anode, leading to higher volumetric and gravimetric energy densities [1]. Lithium thiophosphates are amongst the most promising solid electrolytes to be used in lithium-ion technologies [2–4] and have shown unparalleled ionic conductivities reaching the order of 10^{-2} $S{\cdot}cm^{-1}$ [3,5–8]. This outstanding superiority is closely related to their anionic framework, enabling direct Li hops between adjacent tetrahedral sites with low migration barrier [9,10]. Many sulfide compounds presenting such Li ions percolating networks have been investigated to allow the fastest Li migration, such as Li_3PS_4, $Li_7P_3S_{11}$, $Li_{10}GeP_2S_{12}$ and derivatives [3–6,11–13]. Among all these compounds, Li_6PS_5Cl argyrodite material has received some increasing interest during last decade by showing ionic conductivities of 3–5 $mS{\cdot}cm^{-1}$ [14–16]. However, the narrow electrochemical window of Li_6PS_5Cl leads in practice to unwanted redox reactions during cell cycling, the very first cycles being pointed out for a massive loss of the initial cell capacity [14,15,17,18]. This loss has been attributed to an irreversible reaction from Li_6PS_5Cl that turns toward Li_3PS_4 and LiCl during the first cycle [17,19]. Furthermore, Li_3PS_4 stands as an intermediary compound for reversible redox reactions based on sulfur oxidation during charge ($S^{2-} \rightarrow S^0 + 2e^-$) and phosphorus reduction during discharge ($P^{5+} + 5e^- \rightarrow P^0$). Argyrodite reactivity has been characterized by numerous techniques such as X-ray photoelectronic spectroscopy (XPS) [19–24], X-ray diffraction (XRD) [17,19,24], Raman spectroscopy [19,24], nuclear magnetic resonance (NMR) [17,19], time-of-flight secondary-ion mass spectrometry (ToF-SIMS) [22] and studied using density functional theory (DFT) calculations [17,25] but interestingly, no direct observation has been performed until now. According to the state of the art, redox activity of argyrodite is responsible for the formation of P_2S_5 and elemental sulfur during delithiation and the formation of Li_2S and Li_3P during lithiation. Additional chemical reactivity with the cathode oxides leads to the formation of MS_x (M = Ni, Mn, Co, $1 \leq x \leq 2$), SO_x and PO_x compounds. This work aims to specify the spatial distribution and the nature of intermediary and degradation compounds produced during the cycling of a cell based on Li_6PS_5Cl electrolyte. To focus our comprehension on oxidative mechanisms, only the cathode–electrolyte interface is considered in this article: materials are collected from the composite cathode and our cell is cycled over a high voltage range (2.5–4.1 V) to discard the contribution of reduction mechanisms. In order to perform

* Corresponding author.
E-mail address: naillou@ill.fr (P. Naillou).

https://doi.org/10.1016/j.ensm.2025.104050
Received 5 November 2024; Received in revised form 19 January 2025; Accepted 19 January 2025
Available online 20 January 2025

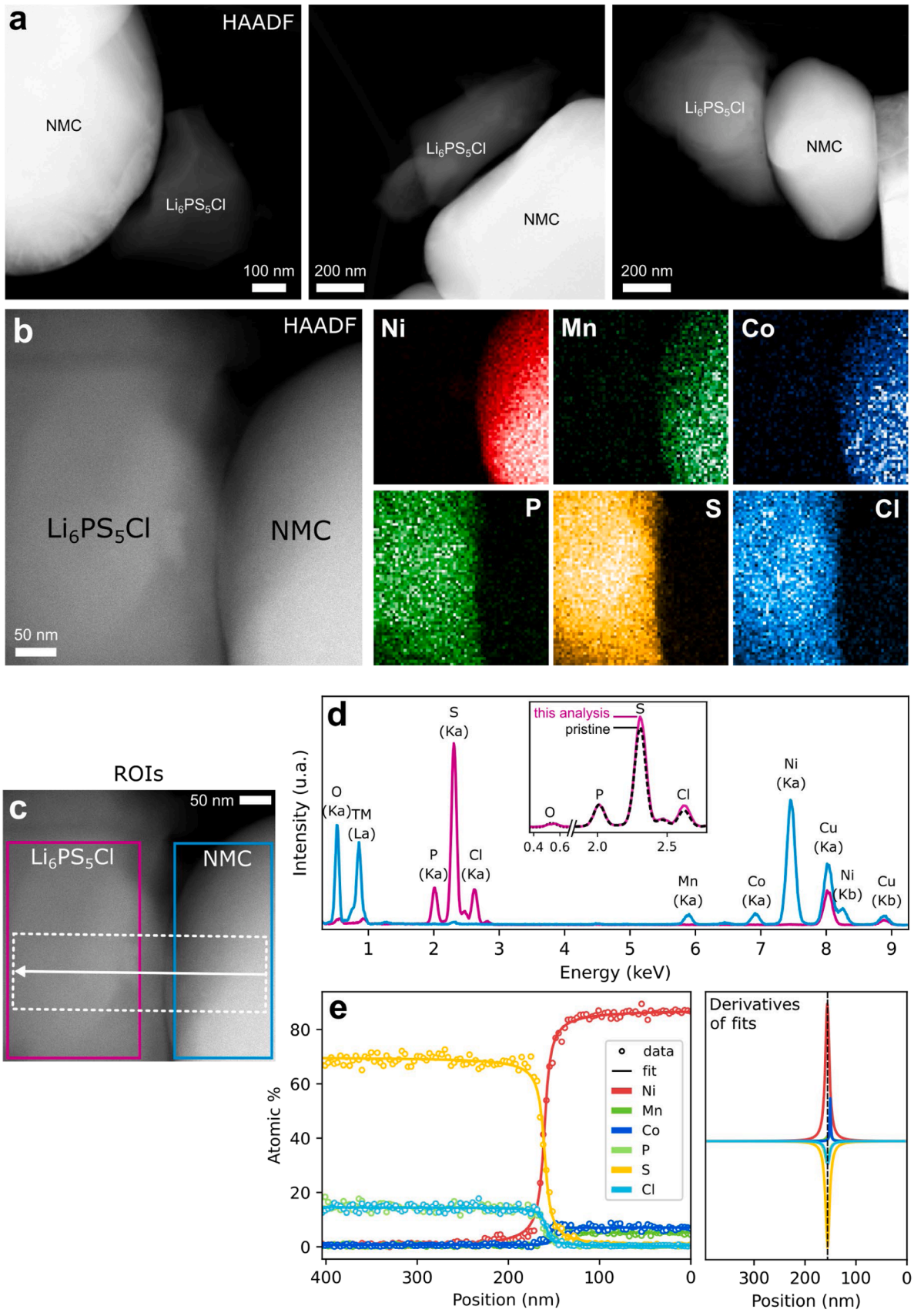

Fig. 1. STEM study of NMC–LPSCl interfaces : (a) HAADF micrographs of several couples of particles; (b) HAADF micrograph and EDX maps of an interface; (c) ROIs over previous study, including (d) EDX spectra for each region and (e) EDX profile along the interface fitted with arctangent functions (derivatives are plotted adjacently).

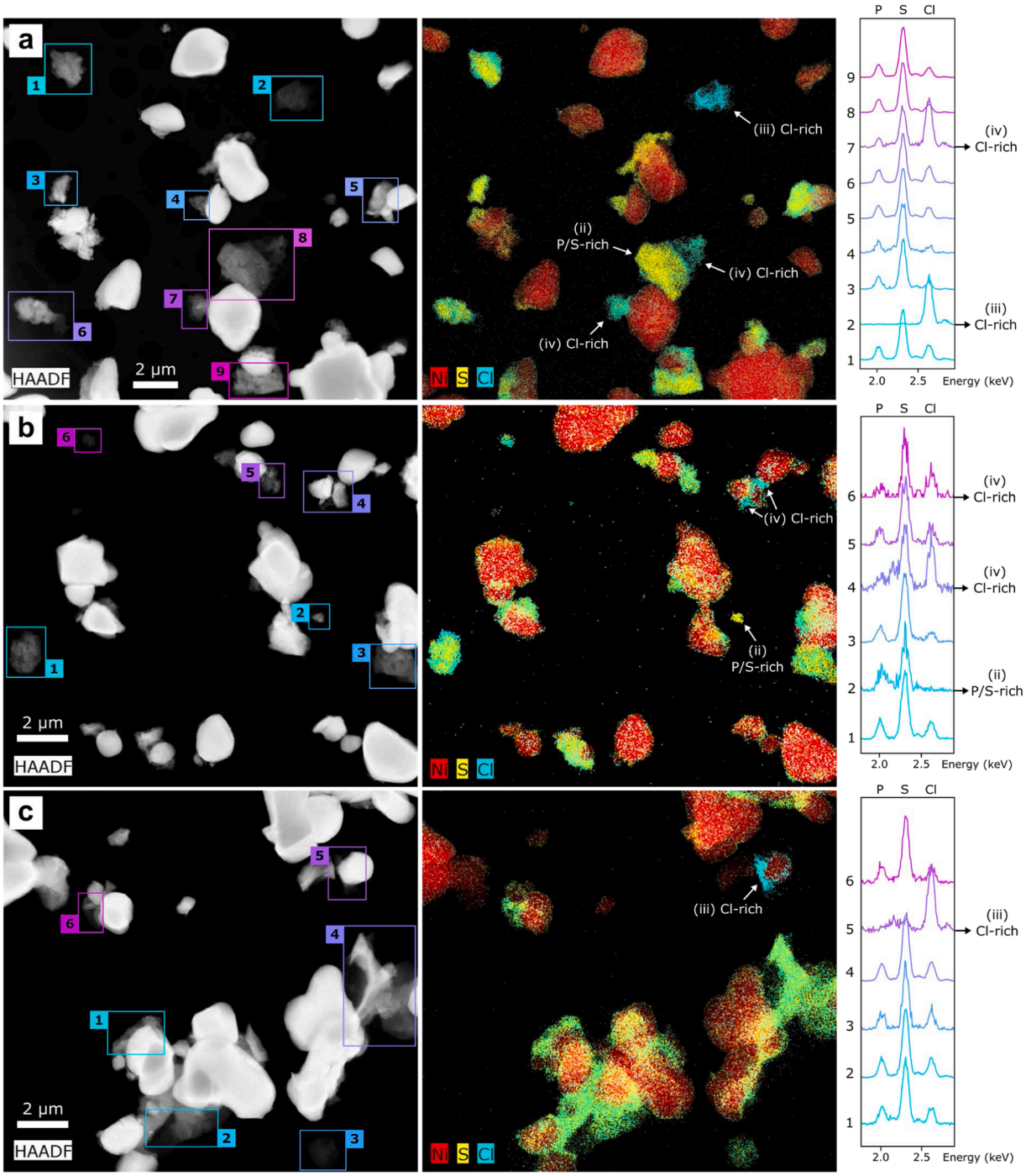

Fig. 2. (a–c) Three low magnification STEM investigations of a cycled LPSCl–NMC cell including : HAADF micrograph (left), EDX overlapped maps for Ni, S, Cl (center) and EDX spectra of corresponding numbered ROIs over the selected energy range for S/P/Cl elements (right). Noteworthy compounds are: (ii) particles showing only a P and S content by EDX with a consistent S/P ratio; (iii) particles showing only a Cl content by EDX; (iv) mixtures of previous compounds, remarked by their important content in Cl.

observations at nanometer scale, we focused on the use of (S)TEM imaging, as well as analytical and diffractive related techniques using a local probe and allowing elemental mappings. Hence, X-ray energy-dispersive spectroscopy (EDX), electron energy loss spectroscopy (EELS) and selected area electron diffraction (SAED) were extensively used over extended areas allowing to ensure the representativeness of the analyses. XPS has been performed to get insights of the chemical composition of the samples and to establish the representativeness of TEM observations, taking advantage of its sensitivity to chemical bonding.

2. Experimental section

Sample preparation – All solid state cells based on NMC and Li_6PS_5Cl have been prepared using Ni-rich NMC ($LiNi_{0.85}Mn_{0.07}Co_{0.08}O_2$) material provided by Umicore and the Li_6PS_5Cl material was prepared at CEA using ball milling followed by annealing. Considering the high sensitivity of argyrodite when exposed to uncontrolled atmospheres [4, 26–29], the pristine state of the material has been assessed by STEM-EDX and SAED (cf. Fig. S2) showing an insignificant oxygen content, highlighting a successful transfer ability from sample to TEM,

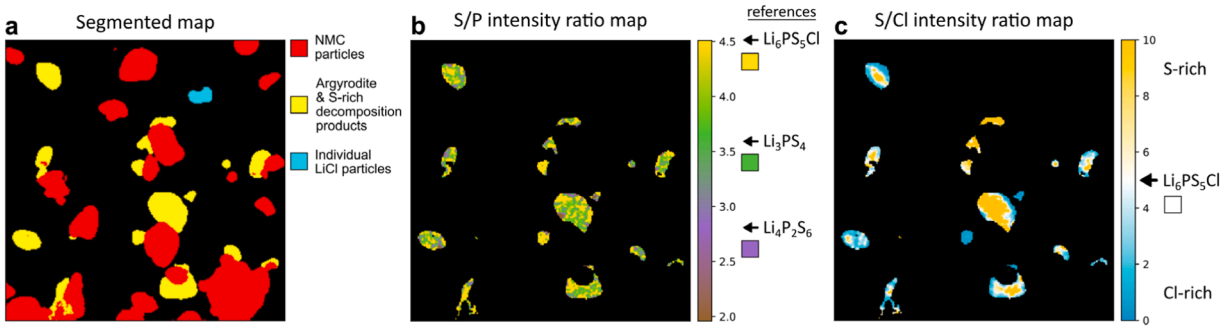

Fig. 3. (a) Segmented map of acquisiton *(a)* from Fig. 2 showing NMC particles (red), argyrodite and S-rich compounds produced during charge (yellow) and individual Cl-rich compounds, further identified as LiCl particles (cyan); **(b)** S/P ratio map plotted from integrating S counts over 2.26–2.37 eV and P counts over 1.97–2.07 eV energy ranges and using a mask from the argyrodite & S-rich compounds segmentation (yellow surface from map *(a)*); **(c)** similar S/Cl ratio map plotted from integrating Cl counts over 2.56–2.71 eV energy range (not representing individual LiCl particles).

and by X-ray Diffraction (cf. Fig. S3), showing traces of remaining compounds LiCl and Li_2S from synthesis with a high overall purity. In the following sections, the materials will be respectively referred as LPSCl and NMC. Full cells using Al current collectors, Li anode, LPSCl electrolyte and LPSCl–NMC (50 vol%/50 vol%) composite cathodes have been assembled in 13 mm-diameter pellets. Composite cathodes have been firstly pressed at room temperature (74 MPa, 3 min), then full cells have been hot pressed under Ar atmosphere (375 MPa, 250 °C, 1 h). Full cells have undergone a single cycle at C/20, 60 °C over 2.5–4.1 V vs Li. Active materials have been recovered from the composite cathode by scraping the surface (cf. Fig. S1 in Supporting Information) and deposited over TEM grids with holey carbon membranes without using any solvent for the powder dispersion. Materials have been handled and stored in Ar-filled glovebox (H_2O, $O_2 < 1$ ppm) and transfers to the TEM were done under air exposure protection using a Gatan 648 double tilt vacuum transfer holder.

Characterization – STEM imaging, EDX, EELS and SAED techniques have been led with FEI Tecnai Osiris TEM equipped with Super-X EDX detector and operated at 200 kV. Bright field (BF, collection semi-angle : 10 mrad), annular dark field (ADF) and high-angle annular dark field (HAADF, collection semi-angle : 50—200 mrad) detectors are used on different occasions to provide different contrast imaging. EDX elemental maps are presented using detected counts as intensity. In this study, we used a reference-based approach for EDX analysis, using various lithium thiophosphates to enable the monitoring and discuss the evolutions observed in the materials of interest. S/P ratio decreases from 5 to 4 while undergoing the $Li_6PS_5Cl \rightarrow Li_3PS_4$ reaction, hence the S/P ratio criterion is used to monitor the evolution. Pristine LPSCl (CEA, S/P = 5), Li_3PS_4 (NEI, S/P = 4) and $Li_4P_2S_6$ (CEA, S/P = 3) reference spectra have been acquired and compared in this study. Each compound and respective spectra are detailed in Supporting Information (Fig. S4). Reduced electron dose conditions are necessary to perform spectroscopic techniques on argyrodite, high spot size and low dwell times are used in order to keep material integrity during data acquisition. While performing EELS experiments, a particular attention is devoted to electron loss near-edge structure (ELNES). Ionization edges for atoms are composed of a fine structure produced by the transition of electrons from the inner-shell state to the conduction band, providing information on oxidation state and chemical environment. EELS spectra have been acquired with a Gatan Imaging Filter Quantum SE. XPS has been performed using a Versaprobe II XPS spectrometer. Charging effects were controlled during analysis with a combination of low-energy electron gun (negative charge) and low-energy argon gun (positive charge). The X-ray source was an Al Kα monochromatic beam (1486.7 eV) and the takeoff angle was set at 45° Pass energy was set to 23.5 eV for high-resolution spectral acquisition, providing an energy resolution of ~0.6 eV Data treatment was performed within the MultiPak software. All spectra were calibrated by using C 1s at 285 eV

3. Results and discussion

3.1. Interfacial stability of uncycled cell

In this part, we aim to determine any chemical reactivity from the pristine fully lithiated NMC with LPSCl. The sample is a composite cathode prepared as described in the experimental section. In Fig. 1, we provide a STEM study of the stability of LPSCl toward NMC material. STEM micrographs of several LPSCl–NMC pairs of particles are presented in Fig. 1a, showing their regular morphology. Great care has been taken on not damaging the materials by electron beam irradiation, especially argyrodite. The elemental distribution across a representative interface between NMC and LPSCl characterized by STEM–EDX mapping is presented in Fig. 1b. The distribution of each chemical element highlights the uniformity of both NMC and LPSCl materials. Two regions of interest (ROIs) have been analyzed by EDX (Fig. 1c). Spectrum for the LPSCl particle facing NMC shows a high sulfur content, very similar to our reference LPSCl, indicating its pristine nature. Fig. 1e presents elemental profiles for each chemical element across the interface fitted with arctangent functions. Such profiles are occasionally used to unveil nanometer-scaled solid interphases compositions between cathode materials and solid electrolytes [30,31]. Derivatives of arctangent fitted functions have been plotted against the elemental profiles, showing one unique location for the interface. Thus, this study shows no evidence of the presence of any interphase or any interdiffusivity. Those observations suggest that LPSCl remains stable against NMC in uncycled cells.

3.2. Redox activity of Li_6PS_5Cl

3.2.1. Compositional screening

The oxidative decomposition limit for LPSCl has been established in previous work at 3.1 V vs Li by XPS and cyclic voltammetry [23] and near 2.0–2.3 V by DFT calculations [17,25]. Hence, Li | LPSCl | LPSCl–NMC cells underwent one cycle between 2.5 and 4.1 V vs Li following the conditions described in the experimental section and show a completely different evolution from the uncycled cell. The voltage profile is provided in Supporting Information Fig. S5. For a better visualization of the consequences of the cycling, several low magnification EDX maps are provided in Fig. 2 highlighting the compositional variety of LPSCl particles through an exhaustive selection of ROIs. EDX maps show at micrometer scale that argyrodite exhibits a strong segregation of chemical elements into different phases. We can observe distinctively the formation of P/S-rich systems and Cl-rich systems: therefore only nickel, sulfur and chlorine are represented on Fig. 2 for an optimal visualization. A compositional screening of the low magnification maps has been performed by selecting ROIs on each entire particle composed of P, S or Cl elements. The corresponding EDX spectra selected over the 1.8–2.9 keV energy range show various compositions such as:

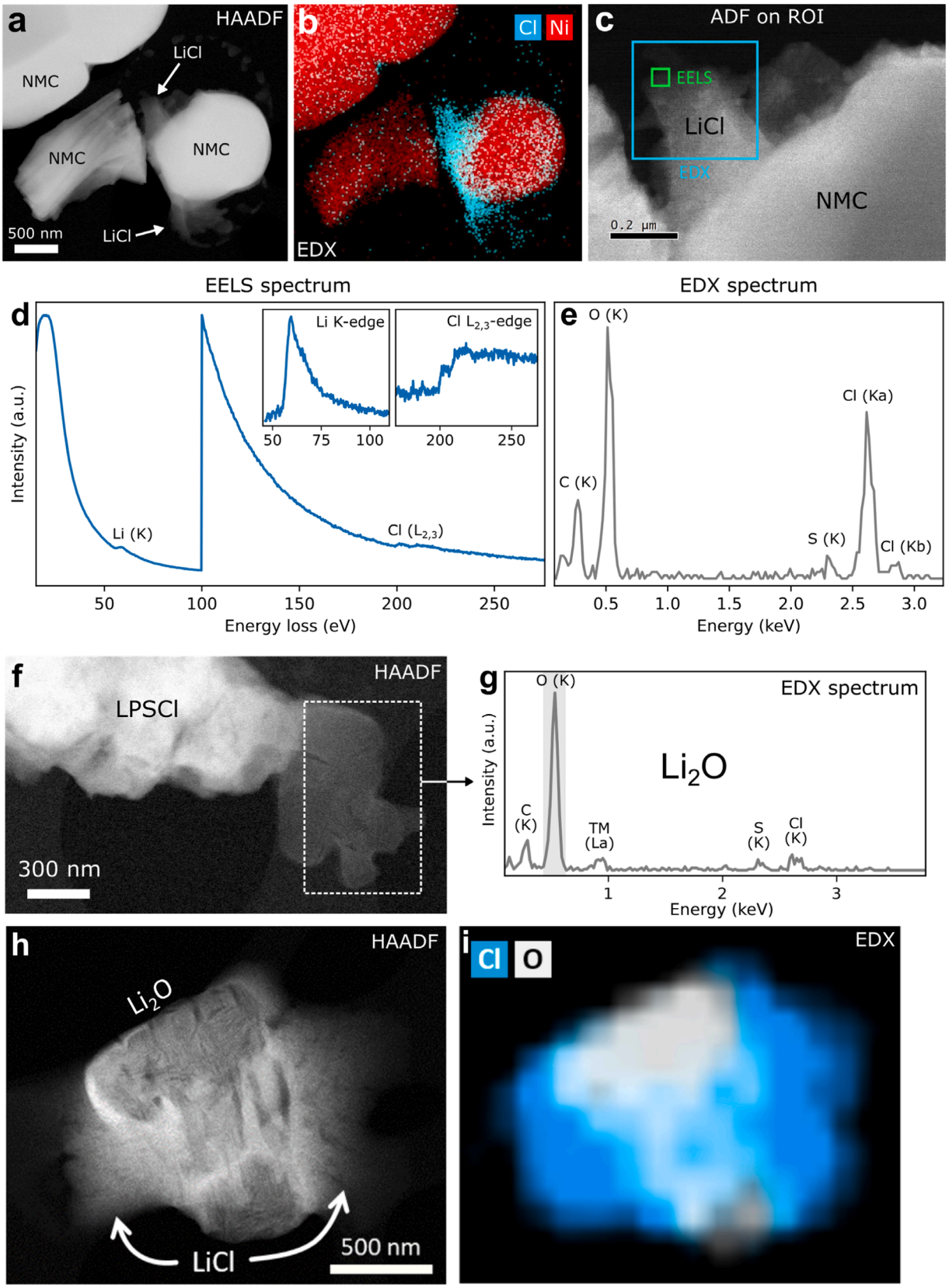

Fig. 4. (a–e) STEM–HAADF, EDX and EELS study of an isolated Cl-rich phase, showing the presence of LiCl and a secondary oxygen-rich compound. An oxygen-rich compound is isolated in study (f–g) presenting low contrast regions where O Kα ray is exclusively detected and is attributed to lithium oxides. (h) HAADF micrograph and (i) EDX map showing the separation of LiCl and O-rich phase.

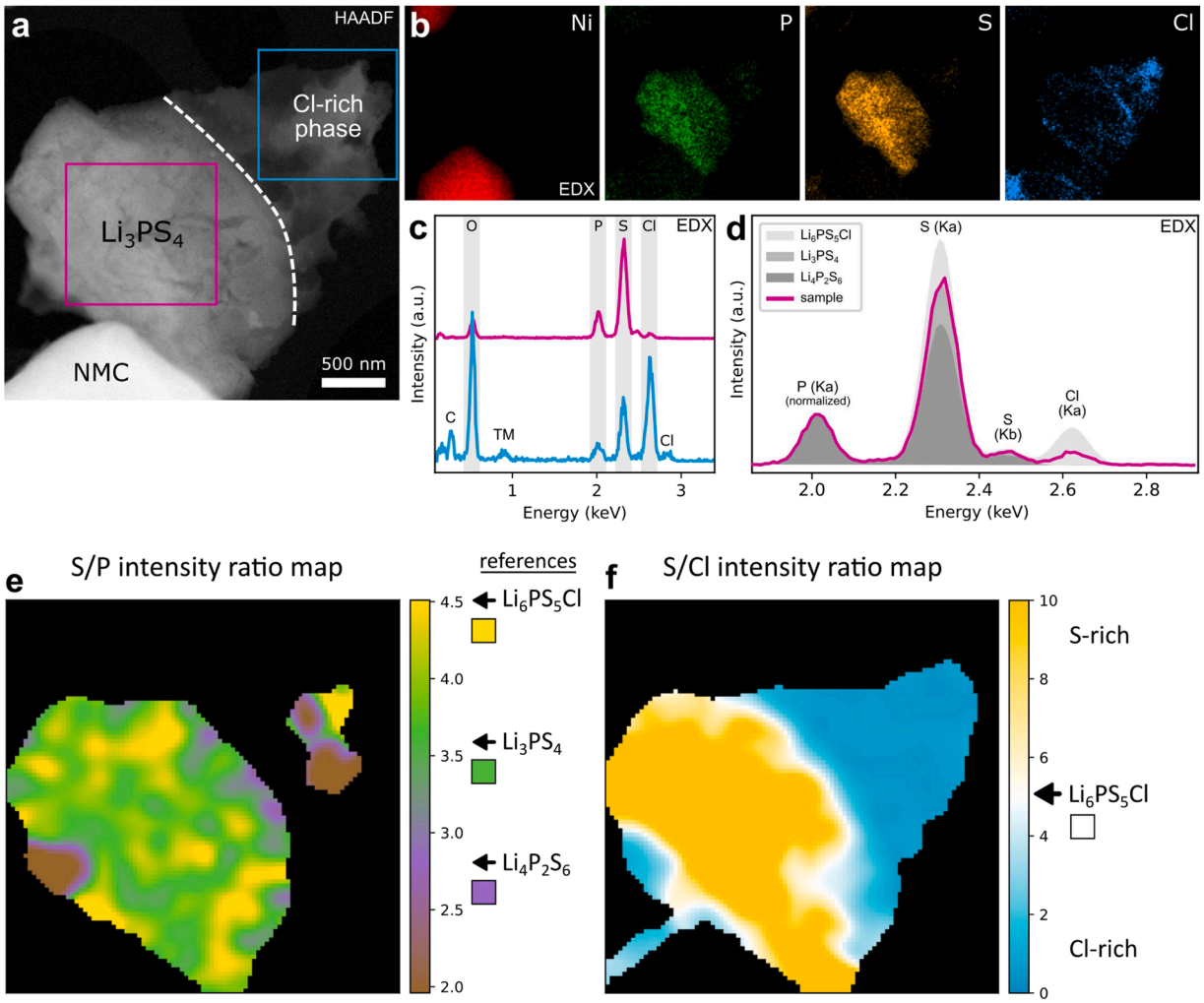

Fig. 5. STEM study on a typical electrolyte particle, including (a) HAADF micrograph, (b) EDX maps and (c) EDX spectra selected over the two main phases composing the particles. The Li_3PS_4 compounds (pink spectra) show high P and S contents and the absence of O and Cl; (d) the EDX spectrum has been compared with lithium thiophosphates references to establish their stoichiometry; (e) S/P intensity ratio map; (f) S/Cl intensity ratio map.

(i) particles containing P/S/Cl elements with a similar stoichiometry to reference argyrodite; (ii) particles containing only P and S with a consistent S/P ratio; (iii) particles containing only Cl; (iv) mixtures of previous compounds, remarked by their important content in Cl. The compounds displayed on Fig. 2 are indexed with numbers (ii–iv) with respect to the latter nomenclature. At this stage, we have no clue on the lithium content and we can only suggest the existence of, at least, a (Li)–P–S phase and a probable LiCl phase. As expected from the voltage range used to cycle our cell, no reduction products are observed, such as Li_2S or Li_3P.

A deeper investigation of the local stoichiometry of the P/S-rich and Cl-rich compounds is proposed in Fig. 3. A segmentation map of NMC particles and compounds produced by argyrodite decomposition using data from Fig. 2a is shown in Fig. 3a. Surfaces and interfaces are not considered in this approach. By focusing only on the surfaces segmented as argyrodite and S-rich products (yellow surfaces in Fig. 3a), elemental ratio maps are calculated and shown in Fig. 3b and Fig. 3c, evidencing the local spatial evolution of S/P and S/Cl ratios, respectively. As argyrodite is highly sensitive to electron beam, a low dwell time has been used during the acquisition of EDX data and therefore the number of photons detected is relatively low at each pixel position, in the order of magnitude of 0–10. Hence, some filtering has been applied to the dataset and is described in Supporting Information Fig. S6. Intensities for each element are calculated using integration windows also described in the supporting material. The S/P ratios calculated for the reference materials using the same integration windows are 4.51 for Li_6PS_5Cl, 3.59 for Li_3PS_4 and 2.81 for $Li_4P_2S_6$, those values are reported on Fig. 3b for a better comprehension. It then turns out that argyrodite with its initial stoichiometry appears yellow while Li_3PS_4 appears green and more oxidized P/S-rich compounds will appear from purple to brown for P_2S_5 compounds with the selected color map. The heterogeneity of the stoichiometry inside each particle is a remarkable point of this analysis, the Li_3PS_4 compound seems to constitute the predominant phase of the material, coexisting with argyrodite and severely oxidized compounds. However, the composition will be discussed later, especially regarding the lithium content. In contrast, the distribution of Cl-rich compounds is more straightforward with a macroscopic phase separation between the (L)PS phase and the Cl-rich phase. S/Cl ratio is calculated at 5.00 for reference argyrodite using the same integration windows, the value is reported on Fig. 3c. Cl-rich regions and S-rich regions are very well demarked, respectively in cyan and yellow, while the regions having the S/Cl stochiometry of pristine argyrodite should appear in white. However, only few regions seem to show the correct S/Cl stoichiometry amongst the visible particles, highlighting a severe transformation of the electrolyte despite what suggests a more global analysis such as in Fig. 2.

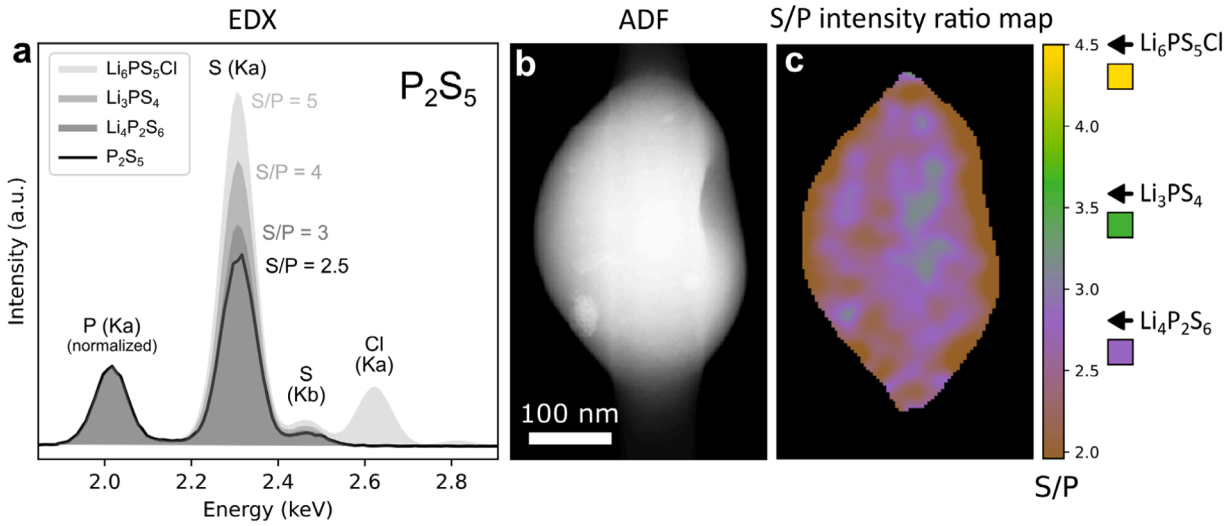

Fig. 6. (a) EDX spectrum of P_2S_5 particle observed in the cycled NMC–LPSCl cell plotted on top of reference spectra from Li_6PS_5Cl, Li_3PS_4 and $Li_4P_2S_6$ compounds; (b) ADF image; (c) S/P intensity ratio map .

3.2.2. *LiCl phase*

The LiCl composition is confirmed by using EELS. In fact, we can easily find isolated Cl-rich particles with null S and P contents, such as particles *a2* and *c5* from Fig. 2. Fig. 4a–*c* shows a magnified view of the latter particle and Fig. 4d–e presents related EELS and EDX spectra. The EELS spectrum shows a strong Li K-edge at 55 eV and a Cl $L_{2,3}$-edge at 200 eV in agreement with the LiCl composition. However, the strong oxygen signal observed in EDX suggests the presence of an additional compound, which has been isolated in some particles such as in Fig. 4f. Li_2O compounds are suspected to be produced during the transformation due to a chemical reaction with the layered oxide cathode. The O content should not come from the atmosphere considering that the cell is prepared in dry room, cycled under vacuum, opened in Ar-filled glovebox and transferred with an atmosphere-protected sample holder. Moreover, the uncycled cell does not show any O content over the argyrodite regions (cf. Fig. 1). The EDX spectrum acquired on the dark contrast region of the particle in Fig. 4g presents exclusively the O Kα ray. Li content is not strictly established due to the high beam sensitivity of the material but Li oxides remain the only relevant explanation to this observation. The distinctiveness of LiCl and Li_2O phases is proved with EDX acquisitions performed with harmless acquisition parameters on isolated particles such as in Fig. 4h–i, in which Cl and O are well separated.

3.2.3. *(L)PS phases*

The (Li)–P–S phases have been characterized by EDX and EELS spectroscopies. Fig. 5 provides an example of a particle presenting a separation into two distinctive phases. A second example provided in Supporting Information Fig. S7 reinforces this observation. The main phase shows a homogeneous distribution of S and P elements (cf. Fig. 5b) and the absence of Cl and O elements according to EDX (cf. Fig. 5b–c). An EELS spectrum acquired on the edge of the P/S-rich phase and provided in Fig. S7 allows to probe the presence of Li observing the Li K-edge at 55 eV simultaneously with L-edges from P and S elements starting at 140 eV, confirming a Li–P–S composition. Using the EDX reference-based approach described in experimental section, we compared the EDX spectra of the observed Li–P–S phase of Fig. 5a with our lithium thiophosphates references in Fig. 5d. By normalizing the spectra by the P intensity, the Li–P–S phase proves to be in a perfect agreement with a Li_3PS_4 stoichiometry. As in Fig. 3b–c, S/P and S/Cl ratio maps are plotted in Fig. 5e–f to discuss the local distribution of the lithium thiophosphates and LiCl compounds. While most of the Li–P–S phase is consistent with a Li_3PS_4 stoichiometry in agreement with the latter conclusion, it is remarkable that severly oxidized compounds are found on the surfaces of the main phase, showing a strong correlation with the presence of LiCl.

Astonishingly, the second phase observed near Li_3PS_4 in the examples of Fig. 5 is a complex mixture showing several redundant features such as very high Cl and O contents and a small P–S content with an even lower S/P ratio than the main Li_3PS_4 phase, as is suggesting the S/Cl ratio map of Fig. 5f. Considering the previous observations, this phase is attributed to a mixture of LiCl, Li_2O and a small fraction of oxidized lithium thiophosphates. LiCl and Li_2O are often associated together, while the main Li_3PS_4 phase shows an insignificant O content. As we can see on low magnification maps from Fig. 2, *a1* and *a8* particles corresponding to the study on Figs. 5a and S7 have a global elemental balance close to the original LPSCl but closer sights to each particle unveils the strong phase separation.

According to the previous studies and DFT calculations performed on argyrodite the formation of Li_3PS_4 compound was expected. We learn through STEM observations in this work that Li_3PS_4 and LiCl are partially entangled in a mixture originating from LPSCl particles. However, other (Li)–P–S particles can present a different stoichiometry, as revealed by the EDX analyses on other regions presented on Fig. 6. The S/P ratio suggests in this case a P_2S_5 compound, which is expected to generate as the most oxidized compound during LPSCl decomposition [17,19,20]. Unlike other compounds studied until now, Li K-edge is not detected for particles with this specific S/P stoichiometry. The S/P map in Fig. 6c indicates that the compound is slightly more oxidized on the surface than in the core.

Fig. 7 presents a summary of the EELS and EDX experiments from the Li | LPSCl | LPSCl–NMC cycled cell. This shows the various compounds formed and originating from LPSCl particles. It includes ADF micrographs of selected particles (cf. Fig. 7c), corresponding EDX spectra over the 1.8–2.9 keV energy range normalized by P Kα ray intensity (cf. Fig. 7a) and corresponding EELS spectra (cf. Fig. 7b), normalized by plasmons intensity between 35 and 100 eV and by P L-edge first feature intensity between 120 and 250 eV While Li_3PS_4 and P_2S_5 are known to be produced during charge due to the narrow electrochemical window of argyrodite, P_2O_5 particles are also found near NMC particles due to chemical reactivity of oxides with sulfides. Their presence is discussed in next section about chemical reactivity. As we can observe, P_2O_5 compound shows a characteristic P L-edge ELNES starting at 140 eV and composed of 4 major features. On EELS spectra for each other thiophosphate compound (P_2S_5, Li_3PS_4, Li_6PS_5Cl), S L-edge is detected from ~160 eV overlapping the reference P L-edge from P_2O_5 and is

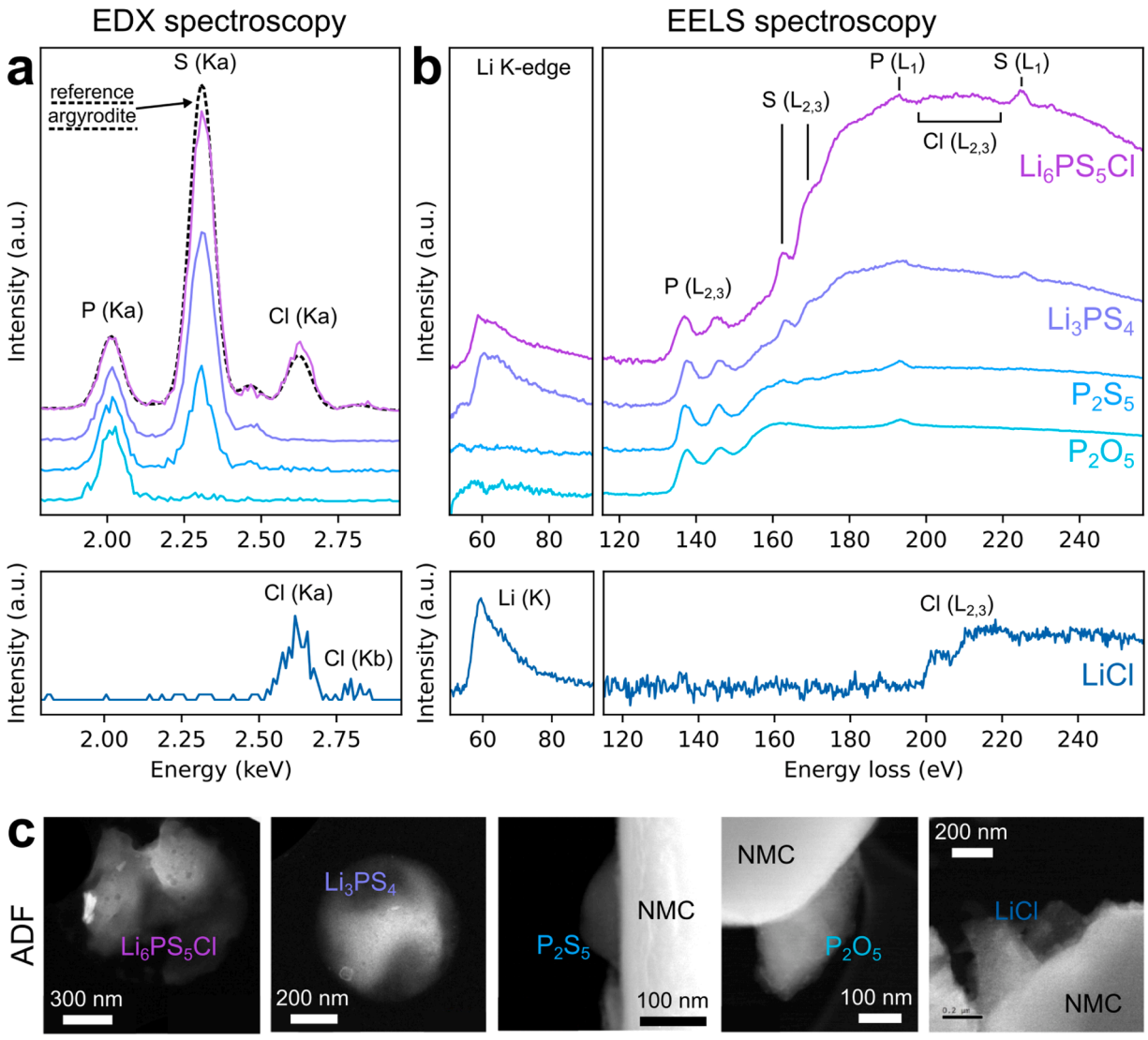

Fig. 7. Series of typical acquisitions from (a) EDX and (b) EELS experiments performed on particles originating from LPSCl in a LPSCl–NMC cycled cell, allowing the identification of the Li_6PS_5Cl, Li_3PS_4, P_2S_5, P_2O_5 and LiCl compounds. EDX and EELS spectra are acquired from particles shown in corresponding (c) ADF micrographs. In top part, EDX spectra are normalized by P Kα intensity and EELS spectra are normalized by plasmons intensity between 35 and 100 eV and by P L-edge first feature intensity between 120 and 250 eV

increasingly more intense as the S/P ratio increases, in agreement with EDX relative S Kα ray intensities.

4. Electrochemical reactivity toward cathode materials

4.1. Phosphorus oxides & transition metals sulfides formation

Due to the strong chemical reactivity of sulfides in presence of oxides, the cathode material particles are leading to the formation of additional compounds such as phosphorus oxides. As we introduced it in previous section and Fig. 7, P_2O_5 compounds have been recurrently observed in the cell and characterized by EDX and EELS. A few examples are provided in Fig. 8, in which two correlated phenomena are observed simultaneously : (i) a S-rich nanometer-scale layer is found on the surface of NMC particles (cf. Fig. 8a–b, c, g–j) and (ii) P_2O_5 particles are observed in contact with NMC and LPSCl materials (cf. Fig. 8a–b, d, *f*). The nature of the phosphorus oxides is firstly suggested by EDX experiments and confirmed by EELS: characteristic features from phosphorus oxides such as P L-edge ELNES are observed [32,33] while no Li K-edge is detected, dispelling the Li_3PO_4 compound. P_2O_5 particles are observed near a S-rich layer. This ~10 nm-thick layer shows *a priori* a significant Ni content. EELS has been performed on the layer and the underlying cathode material (cf. Fig. 8g–j) and shows that : (i) over the cathode region, Li K-edge, Ni $M_{2,3}$-edge and O K-edge are observed in a good agreement with the spectrum of pristine NMC (provided in Supporting Information Fig. S8) and (ii) over the layer region : S L-edge is intense, Ni $M_{2,3}$-edge is observed while Li K-edge is not and O K-edge is barely detectable. The EELS elemental mapping of Li, Ni, S and O elements shows the spatial distribution across the interface confirming that Li is not detected in the layer while Ni element clearly contributes to the layer composition. Hence, in this case such NiS_x compounds are observed because of the highly Ni-rich NMC stoichiometry. Transition metal sulfides could be evenly produced and will be generally referred as MS_x (M = Ni, Mn, Co). The stoichiometry of transition metals in sulfide newly-formed compounds is supported by the analyses of whole particles (~100 nm) found in the cycled cell that present a mixed MS_x/MO_x composition or an overlap of MS_x and MO_x, such as in Fig. 9. Phosphorus oxides are observed in contact with the MS_x particle and the Li K-edge is not detected (cf. Fig. 9d), in agreement with previously established correlations. According to the EDX spectrum (cf. Fig. 9c), transition

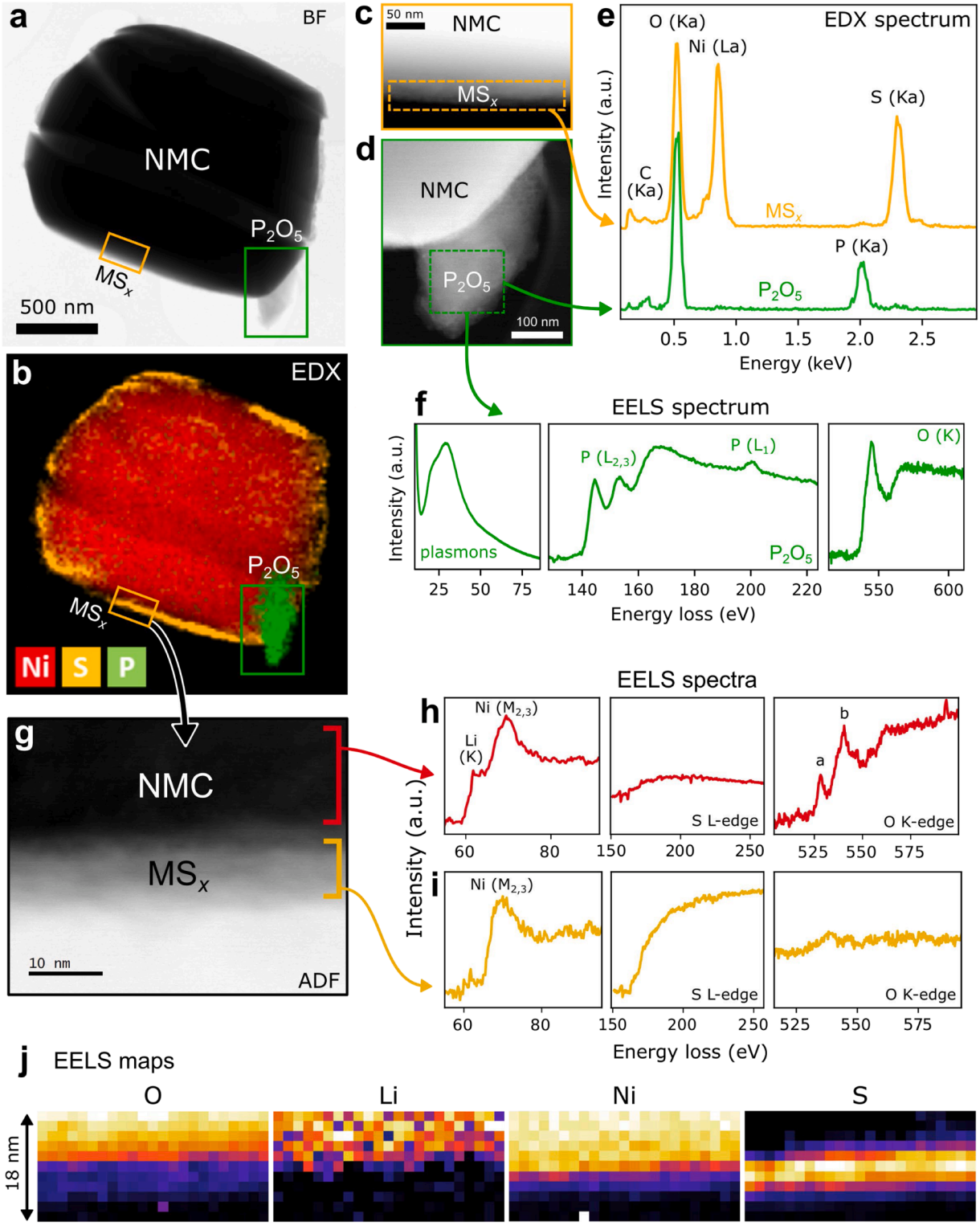

Fig. 8. STEM experiments of the LPSCl–NMC composite cathode from a cycled cell. (a) A BF micrograph and (b) its corresponding EDX maps show (c) a S-rich layer covering the NMC particle and (d) a P_2O_5 compound (ADF images of ROIs). (e) Corresponding EDX spectra of ROIs show their respective elemental composition. (f) EELS spectrum acquired on P_2O_5 particle shows characteristic ELNES for P_2O_5 elements edges and the absence of detection of Li. At the surface of NMC, (g) ADF image shows a variation of contrast between NMC and MS_x layer, respective (h) and (i) EELS spectra show different features. (j) Corresponding EELS maps show the elemental distribution (1.6 nm/pixel). Additional examples of this observation are provided in Supporting Information Fig. S10.

metals are detected in the main particle with the same stoichiometry than the initial NMC composition, confirming the appropriate use of the general form MS_x with M = Ni, Mn, Co. The full EELS spectra are presented in Supporting Information Fig. S9, showing distinctive areas on the particle with mainly a MO_x composition on right edge and mainly a MS_x composition on left edge. This can be interpreted as the progressive sulfidation of delithiated metal oxides in the cell.

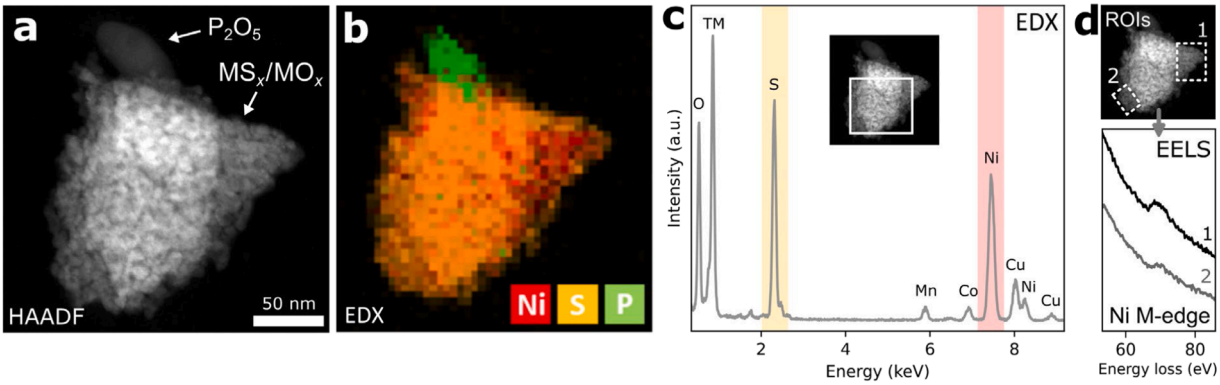

Fig. 9. STEM experiment on a LPSCl–NMC composite cathode from a cycled cell, including: (a) HAADF micrograph and (b) EDX map. Some P_2O_5 compound is visible on top of a large MS_x/MO_x particle; (c) EDX spectrum over the MS_x/MO_x particle; (d) EELS lowloss spectra over two ROIs of the MS_x/MO_x particle, showing the absence of Li K-edge.

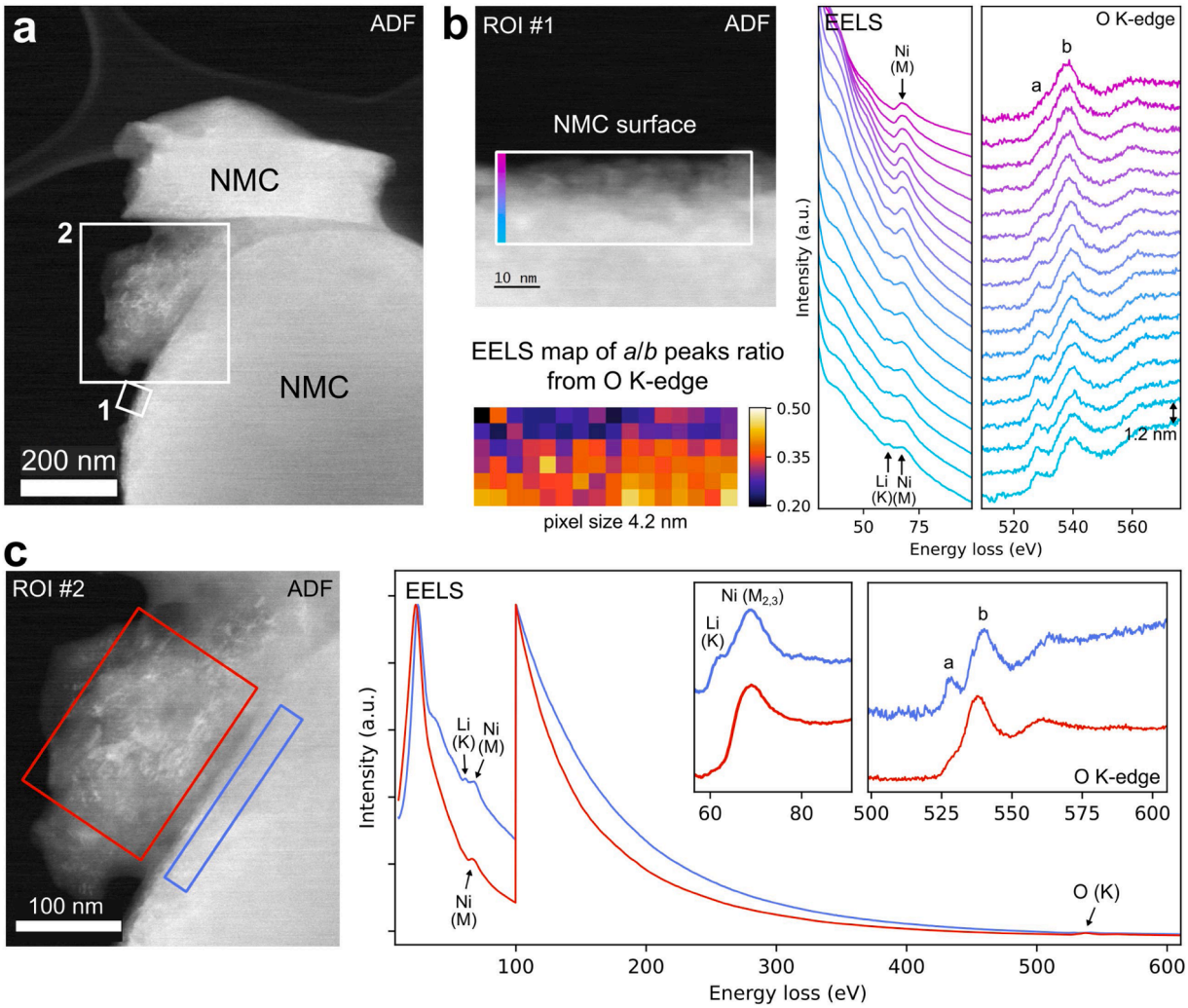

Fig. 10. (a) STEM study of a LPSCl–NMC composite cathode from a cycled cell showing MO_x compounds produced at the surface of NMC particles (b) as surface layer on ROI #1 shown by magnified ADF micrograph, horizontally integrated EELS spectra and EELS map of a/b peaks ratio from O K-edge and (c) as large particles on ROI #2 shown by magnified ADF micrograph and EELS spectra on NMC surface versus on MO_x particle.

4.2. Observation of delithiated transition metals oxides

Meanwhile, a close observation of cathode particles in regions, notoriously not presenting P_2O_5 formation, shows irregular morphologies for NMC materials such as the large surface compound (~200 nm) presented in Fig. 10a, ROI #2. Despite a similar transition metal oxide composition to NMC, EELS spectra unveil the lack of Li in the surface compound and a different ELNES fingerprint than in the

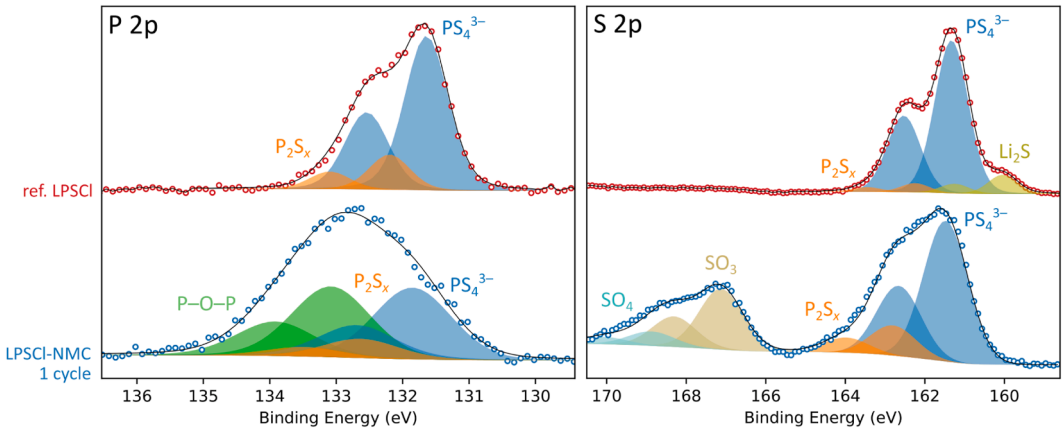

Fig. 11. XPS spectra of reference LPSCl and of the composite cathode from a cycled cell.

underlying NMC (cf. Fig. 10c). Ni $M_{2,3}$-edge is detected over ROI #2 but not Li K-edge, nor the pre-edge peak of O K-edge. However, pristine NMC includes the pre-edge peak, attributed to the $O_{1s} \rightarrow O_{2p}-M_{3d}$ electronic transition, commonly associated to the pristine layered structure described in R-3*m* space group. The decrease of the pre-edge peak is explained by the reduction of neighboring metals and/or the formation of oxygen vacancies, both leading to the modification of the coordination of Ni [34]. The EELS spectrum of pristine NMC used in this study is provided in Supporting Information Fig. S8.

This compound formed upon cycling is identified as NiO_x and is also detected directly on the surface of NMC as a nanometer-scaled layer. In fact, ROI #1 in Fig. 10b presents a continuous EELS study across the surface of NMC with a 1.2 nm increment between spectra and shows the progressive decrease of the pre-edge peak *a* at 528 eV simultaneously with the decrease of Li K-edge at 63 eV The EELS map of the *a*/*b* features ratio from O K-edge is provided and shows the spatial distribution of the NiO_x compound toward NMC (4.2 nm pixel size) over the surface of the particle. This observation assesses the presence of a disordered surface layer of transition metal oxide with a high content of oxygen vacancies over 10 nm at least. The quantification of *x* in NiO_x remains as a delicate point as few techniques are able to confirm the O/Ni ratio at atomic scale and only rocksalt NiO and spinel $LiNi_2O_4$ phases were claimed to be identified for a long time over NMC surfaces. However, new condensed phases have been identified by simulations [35,36] and STEM−EELS [37], completing the $LiNiO_2$−NiO_2−NiO ternary phase diagram. In addition to that, Ni, Mn and Co M-edges are confounded in practice in the 65−75 eV range, the intense contribution at 70 eV observed in our study should be rigorously denominated as a TM M-edges overlap. L-edges of the transition metal have not been acquired in this study as the result of a compromise between energy resolution and energy range in our STEM routine as we wanted to include sulfur and phosphorus L-edges of argyrodite. Hence, a relative quantification method is proposed using O K-edge / TM M-edges ratios and described in Fig. S11. Considering the O/TM value of pristine NMC as a reference, the ratio with the O/TM measured for the observed MO_x surface compound yields $x = 1.68$. This value is close to the β-Ni_5O_8 structure (O/Ni = 1.6) proposed by Ceder's group [35–37]. In the energy window selected to measure the area for quantification of EELS spectra, the bottom energy boundaries exclude carefully the Li K-edge and the O K-edge pre-peak *a*, while the top energy boundaries are relatively low to limit background fitting inaccuracies, particulary strong in lowloss energy range, and multiple scattering inclusion. However, numerous uncertainties persist as multiple phases may coexist within the thick particle studied due to the differential reactivity of transition metals and the spatial resolution of our measurements could not distinguish several phases at atomic scale, nor could the energy resolution of EELS differentiate between the various TM M-edges. Hence, the general form MO_x ($1 \leq x \leq 2$) is prefered in this study as a general term for delithiated transition metal oxides with a significative content of oxygen vacancies.

The Li content of the surface disordered metal oxide is also varying according to the evolution of Li K-edge over the surface of the NMC (cf. Fig. 10b). However, given the convolution of Li K-edge and Ni M-edge, a valuable approach to measure the degree of lithiation in transition metal oxides is using the S_A/S_B method introduced by Kikkawa et al. [38] and previously used for Li K-edges and Co K-edges convoluted as well in cells composed of $LiCoO_2$ cathodes [38,39]. The S_A/S_B surface ratio measured for pristine NMC (cf. Fig. S8e) is 0.51, inferior to the ratios measured for Li/Co in previous studies (0.813–0.99). Using this value as a reference for pristine NMC, the Li/Ni content can be estimated for ROI #1 and ROI #2 in Fig. 10. In ROI #1, the value of S_A/S_B decreases gradually from 0.37 (73 % of pristine NMC) to 0 over 20 nm, the evolution is plotted in Fig. S12. The Li/Ni ratio is measured at 0.31 (61 % of pristine NMC) over ROI #2 on the surface of NMC (cf. Fig. S12), attesting that the NMC is partially delithiated under the MO_x compound.

It is believed through STEM observations that the delithiation of NMC during charge, observed on >20 nm over the surface in this study, leads to the disordering of the surface by the creation of oxygen vacancies over 10 nm, eventually leading to the production of clusters of MO_x compounds originating and detaching from the surface, showing an approximate stoichiometry of $MO_{1.68}$. Then, this disordered metal oxide chemically reacts to MS_x through sulfide compounds exposure such as Li_3PS_4 and/or P_2S_5, which are oxidized to P_2O_5 compounds. Hence, surface MO_x compounds are converted into surface MS_x such as in Fig. 7 while large clusters of MO_x react to form large particles of MS_x such as in Fig. 9 with remaining, uncompletely transformed oxides in some regions. The initial study of the composite cathode before cycling has shown that pristine NMC is not producing any metal sulfides, highlighting the role of cycling in their formation. Delithiated metal oxides are produced only through electrochemical reaction and have been singled out as the origin of metal sulfides and phosphorus oxides in the cycled cell.

5. XPS measurements

As complementary analyses to the previously presented TEM studies at local scale, XPS experiments were performed allowing averaged analyses over wide areas (1.35×1.35 mm^2). Spectra have been acquired on the cycled cell and results are presented in Fig. 11. Pristine LPSCl material shows dominant contributions from PS_4^{3-} tetrahedra with P 2*p* doublet at [131.7, 132.6] eV and S 2p doublet at [161.3, 162.5] eV and some minor disorder established by additional doublets with P 2*p* at [132.4, 133.3] eV and S 2*p* at [162.2, 163.4] eV as well as a slightly reduced environment identified by a doublet at [160.0, 161.2] eV attributed to Li_2S. This Li_2S content is commonly encountered after

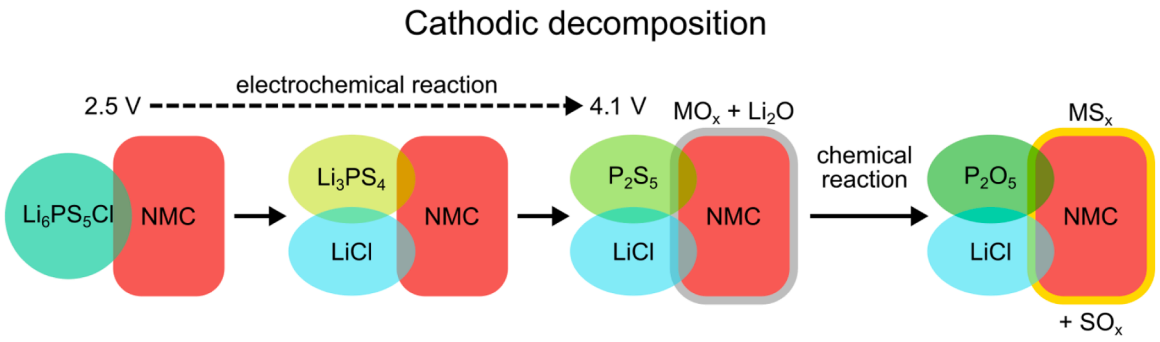

Fig. 12. Global schemes summarizing LPSCl electrochemical and chemical reactivity during charge.

synthesis due to remaining compounds after the milling process [20, 40–42]. However, Li_2S is fully oxidized to lithium thiophosphates during charge above 3–3.5 V[20,42]. Also, such higher energy doublets on P 2*p* and S 2*p* spectra are identified as anionic species generally such as $P_2S_6^{4-}$ or $P_2S_7^{4-}$ moieties [43,44], resulting from the bridging of PS_4^{3-} tetrahedra through redox activation [44–46]. However, the composite cathode of a cycled cell shows a major transformation of argyrodite identified by the increase of the intensity of P_2S_x doublets, the emergence of a third doublet on P 2*p* spectrum attributed to P_2O_5 compound and of two doublets at high energy on S 2*p* spectrum attributed to SO_x. The binding energies of P_2S_x moieties are fluctuating with the S/P stoichiometry as shown by comprehensive related studies [44]. Some margin of freedom should be kept in the ~162.2–163.0 eV range (S $2p_{3/2}$) and in the ~132.3–133.5 eV range (P $2p_{3/2}$) when fitting contributions while such complex mixtures of lithium thiophosphates are encountered.

The contributions of MS_x compounds are expected in S 2*p* spectrum, however their convolution with PS_4^{3-} doublet is a major drawback for their inclusion. Previous XPS works in literature on argyrodite usually do not include MS_x on XPS spectra for similar reason, as every NiS_x compound for instance should lead to a doublet between 161.2 and 161.6 eV (S $2p_{3/2}$) and at 162.8 eV (S $2p_{1/2}$) according to other works [47]. Those binding energies are practically merged with PS_4^{3-} doublet, fitted in this study at [161.5, 162.7] eV. In order to reach a representative deconvolution of the contributions, PS_4^{3-} doublet on S 2*p* spectrum has been constrained to fulfill a 1:4 ratio with PS_4^{3-} doublet from P 2*p* spectrum as we know the S/P ratio of this moeity. The P_2S_x moeity is assumed to fulfill a ratio between 1:3 and 1:3.5 as P_2S_x compounds are known to be either $P_2S_6^{4-}$ or $P_2S_7^{4-}$ in Li_3PS_4. This *a priori* knowledge imposes the input of an additionnal contribution at higher energies, which is correctly filled by the doublet for P–O–P bounds reported at similar binding energies [48] and fitted in this study at [133.1, 133.9] eV. This constrain yields a S/P ratio of 1 : 3.18 for P_2S_x doublet, which is in agreement with the expected bounds $6 \leq x \leq 7$. This observation highlights the significance of P–O–P bounds observed at higher energies, confirming the representativity of STEM observations. We choosed not to include any MS_x doublet in the S 2*p* spectrum despite we believe a contribution exists at nearly same binding energies than PS_4^{3-} doublet.

XPS results are in agreement with TEM observations: the increase of P_2S_x doublets is directly connected to the formation of Li_3PS_4 and P_2S_5 compounds through redox activation, while P_2O_5 is representatively found in XPS as well as in TEM as a result of the chemical reactivity of (lithium/) thiophosphates with cathode oxides. Main observations have been performed during this study, emphasizing the correlation between the formation of surface MO_x on NMC through cycling, leading to the formation of MS_x and P_2O_5. Main results of this study are represented in Fig. 12 top scheme.

6. Conclusion

This work aimed to specify the nature and distribution of compounds formed during the charge of a LPSCl-based cell by studying the LPSCl–NMC composite cathode through TEM. LPSCl decomposes to LiCl, Li_3PS_4 and P_2S_5 compounds through a complex phase separation. The Cl-rich phase is mostly a mixture of LiCl, Li_2O and a constant smaller fraction of more oxidized thiophosphates while the main Li_3PS_4 phase do not show any significant oxygen content. Astonishingly, LPSCl shows a good stability with the NMC outside of any electrochemical solicitation. Oxidized thiophosphates are the main origin of further reactivity with the NMC. Upon cycling, the surface of the NMC encounters structural disordering and the increase of oxygen vacancies over 10 nm for observed surfaces, leading to the formation of delithiated transition metal oxides MO_x. Such MO_x are produced over the surface of NMC and eventually detach from the surface to form large clusters (up to ~200 nm), quantitative EELS has been used to identify a ratio O/TM of 1.68, suggesting the presence of compounds such as known Ni_5O_8 given the high Ni content of the cathode. MO_x compounds react to MS_x through the exposition to (lithium/) thiophosphates. Those are oxidized to P_2O_5, showing a strong spatial correlation with MS_x formation during our study. Given the unique results brought by this approach using STEM –EDX and –EELS in the understanding of cathode–electrolyte interfaces, we highly encourage the use of STEM as a powerful analytical tool for the study of interfaces in lithium batteries.

CRediT authorship contribution statement

Paul Naillou: Writing – original draft, Visualization, Software, Methodology, Investigation, Formal analysis, Conceptualization. **Adrien Boulineau:** Writing – review & editing, Validation, Supervision, Project administration, Methodology, Conceptualization. **Eric De Vito:** Writing – review & editing, Validation, Software, Investigation, Formal analysis. **Enora Lavanant:** Validation, Resources, Project administration. **Philippe Azaïs:** Writing – review & editing, Validation, Supervision, Project administration, Funding acquisition.

Declaration of competing interest

The authors declare the following financial interests/personal relationships which may be considered as potential competing interests:

Paul Naillou reports financial support was provided by Umicore. Paul Naillou reports financial support was provided by French National Research Agency. If there are other authors, they declare that they have no known competing financial interests or personal relationships that could have appeared to influence the work reported in this paper.

Acknowledgments

The authors gratefully acknowledge the financial support of Umicore. This work, carried out on the Platform for Nanocharacterisation (PFNC), was supported by the “Recherche Technologique de Base” and “France 2030 - ANR-22-PEEL-0014” programs of the French National Research Agency (ANR).

Supplementary materials

Supplementary material associated with this article can be found, in the online version, at doi:10.1016/j.ensm.2025.104050.

References

[1] J. Janek, W.G. Zeier, A solid future for battery development, Nat. Energy 1 (9) (2016) 16141, https://doi.org/10.1038/nenergy.2016.141.

[2] C. Wang, J. Liang, Y. Zhao, M. Zheng, X. Li, X. Sun, All-solid-state lithium batteries enabled by sulfide electrolytes: from fundamental research to practical engineering design, Energy Environ. Sci. 14 (5) (2021) 2577–2619, https://doi.org/10.1039/D1EE00551K.

[3] C. Yu, F. Zhao, J. Luo, L. Zhang, X. Sun, Recent development of lithium argyrodite solid-state electrolytes for solid-state batteries: synthesis, structure, stability and dynamics, Nano Energy 83 (2021) 105858, https://doi.org/10.1016/j.nanoen.2021.105858.

[4] R. Guo, K. Zhang, W. Zhao, Z. Hu, S. Li, Y. Zhong, R. Yang, X. Wang, J. Wang, C. Wu, Y. Bai, Interfacial challenges and strategies toward practical sulfide-based solid-state lithium batteries, Energy Mater. Adv. 4 (2023) 0022, https://doi.org/10.34133/energymatadv.0022.

[5] N. Kamaya, K. Homma, Y. Yamakawa, M. Hirayama, R. Kanno, M. Yonemura, T. Kamiyama, Y. Kato, S. Hama, K. Kawamoto, A. Mitsui, A lithium superionic conductor, Nat. Mater. 10 (9) (2011) 682–686, https://doi.org/10.1038/nmat3066.

[6] Y. Kato, S. Hori, T. Saito, K. Suzuki, M. Hirayama, A. Mitsui, M. Yonemura, H. Iba, R. Kanno, High-power all-solid-state batteries using sulfide superionic conductors, Nat. Energy 1 (4) (2016) 16030, https://doi.org/10.1038/nenergy.2016.30.

[7] P. Adeli, J.D. Bazak, K.H. Park, I. Kochetkov, A. Huq, G.R. Goward, L.F. Nazar, Boosting solid-state diffusivity and conductivity in lithium superionic argyrodites by halide substitution, Angew. Chem. Int. Ed. 58 (26) (2019) 8681–8686, https://doi.org/10.1002/anie.201814222.

[8] Y.-K. Sun, S.-T. Myung, M.-H. Kim, J. Prakash, K. Amine, Synthesis and characterization of $Li[(Ni_{0.8}Co_{0.1}Mn_{0.1})_{0.8}(Ni_{0.5}Mn_{0.5})_{0.2}]O_2$ with the microscale core−shell structure as the positive electrode material for lithium batteries, J. Am. Chem. Soc. 127 (38) (2005) 13411–13418, https://doi.org/10.1021/ja053675g.

[9] Y. Wang, W.D. Richards, S.P. Ong, L.J. Miara, J.C. Kim, Y. Mo, G. Ceder, Design principles for solid-state lithium superionic conductors, Nat. Mater. 14 (10) (2015) 1026–1031, https://doi.org/10.1038/nmat4369.

[10] I. Hanghofer, M. Brinek, S.L. Eisbacher, B. Bitschnau, M. Volck, V. Hennige, I. Hanzu, D. Rettenwander, H.M.R. Wilkening, Substitutional disorder: structure and ion dynamics of the argyrodites Li_6PS_5Cl, Li_6PS_5Br and Li_6PS_5I, Phys. Chem. Chem. Phys. 21 (16) (2019) 8489–8507, https://doi.org/10.1039/C9CP00664H.

[11] Z. Liu, W. Fu, E.A. Payzant, X. Yu, Z. Wu, N.J. Dudney, J. Kiggans, K. Hong, A. J. Rondinone, C. Liang, Anomalous high ionic conductivity of nanoporous β-Li_3PS_4, J. Am. Chem. Soc. 135 (3) (2013) 975–978, https://doi.org/10.1021/ja3110895.

[12] H. Yamane, M. Shibata, Y. Shimane, T. Junke, Y. Seino, S. Adams, K. Minami, A. Hayashi, M. Tatsumisago, Crystal structure of a superionic conductor, $Li_7P_3S_{11}$, Solid State Ion. 178 (15–18) (2007) 1163–1167, https://doi.org/10.1016/j.ssi.2007.05.020.

[13] Y. Seino, T. Ota, K. Takada, A. Hayashi, M. Tatsumisago, A sulphide lithium super ion conductor is superior to liquid ion conductors for use in rechargeable batteries, Energy Environ. Sci. 7 (2) (2014) 627–631, https://doi.org/10.1039/C3EE41655K.

[14] S. Wang, Y. Zhang, X. Zhang, T. Liu, Y.-H. Lin, Y. Shen, L. Li, C.-W. Nan, High-conductivity argyrodite Li_6PS_5Cl solid electrolytes prepared via optimized sintering processes for all-solid-state lithium–sulfur batteries, ACS Appl. Mater. Interfaces 10 (49) (2018) 42279–42285, https://doi.org/10.1021/acsami.8b15121.

[15] C. Yu, S. Ganapathy, J. Hageman, L. Van Eijck, E.R.H. Van Eck, L. Zhang, T. Schwietert, S. Basak, E.M. Kelder, M. Wagemaker, Facile synthesis toward the optimal structure-conductivity characteristics of the argyrodite Li_6PS_5Cl solid-state electrolyte, ACS Appl. Mater. Interfaces 10 (39) (2018) 33296–33306, https://doi.org/10.1021/acsami.8b07476.

[16] C. Zhao, M. Lyu, C. Bi, S. Huo, S. Li, W. Xue, Synthesis of high ionic conductivity Li6PS5Cl solid electrolyte by second sintering process, Results Chem. 4 (2022) 100468, https://doi.org/10.1016/j.rechem.2022.100468.

[17] T.K. Schwietert, V.A. Arszelewska, C. Wang, C. Yu, A. Vasileiadis, N.J.J. de Klerk, J. Hageman, T. Hupfer, I. Kerkamm, Y. Xu, E. van der Maas, E.M. Kelder, S. Ganapathy, M. Wagemaker, Clarifying the relationship between redox activity and electrochemical stability in solid electrolytes, Nat. Mater. 19 (4) (2020) 428–435, https://doi.org/10.1038/s41563-019-0576-0.

[18] C. Yu, L. van Eijck, S. Ganapathy, M. Wagemaker, Synthesis, structure and electrochemical performance of the argyrodite Li_6PS_5Cl solid electrolyte for Li-ion solid state batteries, Electrochim. Acta 215 (2016) 93–99, https://doi.org/10.1016/j.electacta.2016.08.081.

[19] D.H.S. Tan, E.A. Wu, H. Nguyen, Z. Chen, M.A.T. Marple, J.-M. Doux, X. Wang, H. Yang, A. Banerjee, Y.S. Meng, Elucidating reversible electrochemical redox of Li_6PS_5Cl solid electrolyte, ACS Energy Lett. 4 (10) (2019) 2418–2427, https://doi.org/10.1021/acsenergylett.9b01693.

[20] J. Auvergniot, A. Cassel, D. Foix, V. Viallet, V. Seznec, R. Dedryvère, Redox activity of argyrodite Li_6PS_5Cl electrolyte in all-solid-state Li-ion battery: an XPS study, Solid State Ion. 300 (2017) 78–85, https://doi.org/10.1016/j.ssi.2016.11.029.

[21] J. Auvergniot, A. Cassel, J.-B. Ledeuil, V. Viallet, V. Seznec, R. Dedryvère, Interface stability of argyrodite Li_6PS_5Cl toward $LiCoO_2$, $LiNi_{1/3}Co_{1/3}Mn_{1/3}O_2$, and $LiMn_2O_4$ in bulk all-solid-state batteries, Chem. Mater. 29 (9) (2017) 3883–3890, https://doi.org/10.1021/acs.chemmater.6b04990.

[22] F. Walther, R. Koerver, T. Fuchs, S. Ohno, J. Sann, M. Rohnke, W.G. Zeier, J. Janek, Visualization of the interfacial decomposition of composite cathodes in argyrodite-based all-solid-state batteries using time-of-flight secondary-ion mass spectrometry, Chem. Mater. 31 (10) (2019) 3745–3755, https://doi.org/10.1021/acs.chemmater.9b00770.

[23] G.F. Dewald, S. Ohno, M.A. Kraft, R. Koerver, P. Till, N.M. Vargas-Barbosa, J. Janek, W.G. Zeier, Experimental assessment of the practical oxidative stability of lithium thiophosphate solid electrolytes, Chem. Mater. 31 (20) (2019) 8328–8337, https://doi.org/10.1021/acs.chemmater.9b01550.

[24] A. Banerjee, H. Tang, X. Wang, J.-H. Cheng, H. Nguyen, M. Zhang, D.H.S. Tan, T. A. Wynn, E.A. Wu, J.-M. Doux, T. Wu, L. Ma, G.E. Sterbinsky, M.S. D'Souza, S. P. Ong, Y.S. Meng, Revealing nanoscale solid–solid interfacial phenomena for long-life and high-energy all-solid-state batteries, ACS Appl. Mater. Interfaces 11 (46) (2019) 43138–43145, https://doi.org/10.1021/acsami.9b13955.

[25] Y. Zhu, X. He, Y. Mo, Origin of outstanding stability in the lithium solid electrolyte materials: insights from thermodynamic analyses based on first-principles calculations, ACS Appl. Mater. Interfaces 7 (42) (2015) 23685–23693, https://doi.org/10.1021/acsami.5b07517.

[26] J. Liang, X. Li, C. Wang, J.T. Kim, R. Yang, J. Wang, X. Sun, Current status and future directions in environmental stability of sulfide solid-state electrolytes for all-solid-state batteries, Energy Mater. Adv. 4 (2023) 0021, https://doi.org/10.34133/energymatadv.0021.

[27] P. Naillou, A. Boulineau, E. De Vito, R. Ramos, P. Azaïs, Evidencing phase transformations of Li_6PS_5Cl argyrodite under ambient air and dry room exposure, ACS Appl. Mater. Interfaces 16 (40) (2024) 53855–53863, https://doi.org/10.1021/acsami.4c11458.

[28] T.A. Yersak, Y. Zhang, F. Hao, M. Cai, Moisture stability of sulfide solid-state electrolytes, Front. Energy Res. 10 (2022) 882508, https://doi.org/10.3389/fenrg.2022.882508.

[29] X. Randrema, I. Leteyi Mfiban, M. Soler, I. Profatilova, M. Berthault, R. Ramos, J. Lavie, E. De Vito, L. Blanc, S. Diry, S. Launois, V. Tarnopolskiy, M. Reytier, J. Colin, C. Barchasz, S. Liatard, Towards a practical use of sulfide solid electrolytes in solid-state batteries: impact of dry room exposure on H_2S release and material properties, Batter. Supercaps 7 (1) (2024) e202300380, https://doi.org/10.1002/batt.202300380.

[30] G. Vardar, W.J. Bowman, Q. Lu, J. Wang, R.J. Chater, A. Aguadero, R. Seibert, J. Terry, A. Hunt, I. Waluyo, D.D. Fong, A. Jarry, E.J. Crumlin, S.L. Hellstrom, Y.-M. Chiang, B. Yildiz, Structure, chemistry, and charge transfer resistance of the interface between $Li_7La_3Zr_2O_{12}$ electrolyte and $LiCoO_2$ cathode, Chem. Mater. 30 (18) (2018) 6259–6276, https://doi.org/10.1021/acs.chemmater.8b01713.

[31] A. Sakuda, A. Hayashi, M. Tatsumisago, Interfacial observation between $LiCoO_2$ electrode and Li_2S–P_2S_5 solid electrolytes of all-solid-state lithium secondary batteries using transmission electron microscopy, Chem. Mater. 22 (3) (2010) 949–956, https://doi.org/10.1021/cm901819c.

[32] Y. Huang, J. Qiao, K. He, S. Bliznakov, E. Sutter, X. Chen, D. Luo, F. Meng, D. Su, J. Decker, W. Ji, R.S. Ruoff, P. Sutter, Interaction of black phosphorus with oxygen and water, Chem. Mater. 28 (22) (2016) 8330–8339, https://doi.org/10.1021/acs.chemmater.6b03592.

[33] D. Cheng, T.A. Wynn, X. Wang, S. Wang, M. Zhang, R. Shimizu, S. Bai, H. Nguyen, C. Fang, M. Kim, W. Li, B. Lu, S.J. Kim, Y.S. Meng, Unveiling the stable nature of the solid electrolyte interphase between lithium metal and LiPON via cryogenic electron microscopy, Joule 4 (11) (2020) 2484–2500, https://doi.org/10.1016/j.joule.2020.08.013.

[34] D. Qian, B. Xu, M. Chi, Y.S. Meng, Uncovering the roles of oxygen vacancies in cation migration in lithium excess layered oxides, Phys. Chem. Chem. Phys. 16 (28) (2014) 14665–14668, https://doi.org/10.1039/C4CP01799D.

[35] H. Das, A. Urban, W. Huang, G. Ceder, First-principles simulation of the (Li–Ni–vacancy)O phase diagram and its relevance for the surface phases in Ni-rich Li-ion cathode materials, Chem. Mater. 29 (18) (2017) 7840–7851, https://doi.org/10.1021/acs.chemmater.7b02546.

[36] P. Xiao, T. Shi, W. Huang, G. Ceder, Understanding surface densified phases in Ni-rich layered compounds, ACS Energy Lett. 4 (4) (2019) 811–818, https://doi.org/10.1021/acsenergylett.9b00122.

[37] P. Mukherjee, P. Lu, N. Faenza, N. Pereira, G. Amatucci, G. Ceder, F. Cosandey, Atomic structure of surface-densified phases in Ni-rich layered compounds, ACS Appl. Mater. Interfaces 13 (15) (2021) 17478–17486, https://doi.org/10.1021/acsami.1c00143.

[38] J. Kikkawa, S. Terada, A. Gunji, T. Nagai, K. Kurashima, K. Kimoto, Chemical states of overcharged $LiCoO_2$ particle surfaces and interiors observed using electron energy-loss spectroscopy, J. Phys. Chem. C 119 (28) (2015) 15823–15830, https://doi.org/10.1021/acs.jpcc.5b02303.

[39] Y. Nomura, K. Yamamoto, M. Fujii, T. Hirayama, E. Igaki, K. Saitoh, Dynamic imaging of lithium in solid-state batteries by operando electron energy-loss spectroscopy with sparse coding, Nat. Commun. 11 (1) (2020) 2824, https://doi.org/10.1038/s41467-020-16622-w.

[40] F. Strauss, D. Stepien, J. Maibach, L. Pfaffmann, S. Indris, P. Hartmann, T. Brezesinski, Influence of electronically conductive additives on the cycling performance of argyrodite-based all-solid-state batteries, RSC Adv. 10 (2) (2020) 1114–1119, https://doi.org/10.1039/C9RA10253A.

[41] X. Randrema, C. Barcha, M. Chakir, V. Viallet, M. Morcrette, A detailed characterisation study of Li6PS5Cl ionic conductors from several synthetic routes,

Solid State Sci. 118 (2021) 106681, https://doi.org/10.1016/j.solidstatesciences.2021.106681.
[42] S. Wang, M. Tang, Q. Zhang, B. Li, S. Ohno, F. Walther, R. Pan, X. Xu, C. Xin, W. Zhang, L. Li, Y. Shen, F.H. Richter, J. Janek, C. Nan, Lithium argyrodite as solid electrolyte and cathode precursor for solid-state batteries with long cycle life, Adv. Energy Mater. 11 (31) (2021) 2101370, https://doi.org/10.1002/aenm.202101370.
[43] K. Ohara, A. Mitsui, M. Mori, Y. Onodera, S. Shiotani, Y. Koyama, Y. Orikasa, M. Murakami, K. Shimoda, K. Mori, T. Fukunaga, H. Arai, Y. Uchimoto, Z. Ogumi, Structural and electronic features of binary Li2S-P2S5 glasses, Sci. Rep. 6 (1) (2016) 21302, https://doi.org/10.1038/srep21302.
[44] C. Dietrich, R. Koerver, M.W. Gaultois, G. Kieslich, G. Cibin, J. Janek, W.G. Zeier, Spectroscopic characterization of lithium thiophosphates by XPS and XAS – a model to help monitor interfacial reactions in all-solid-state batteries, Phys. Chem. Chem. Phys. 20 (30) (2018) 20088–20095, https://doi.org/10.1039/C8CP01968A.
[45] T. Hakari, M. Nagao, A. Hayashi, M. Tatsumisago, All-solid-state lithium batteries with Li3PS4 glass as active material, J. Power Sources 293 (2015) 721–725, https://doi.org/10.1016/j.jpowsour.2015.05.073.
[46] R. Koerver, F. Walther, I. Aygün, J. Sann, C. Dietrich, W.G. Zeier, J. Janek, Redox-active cathode interphases in solid-state batteries, J. Mater. Chem. A 5 (43) (2017) 22750–22760, https://doi.org/10.1039/C7TA07641J.
[47] R. Karthikeyan, D. Thangaraju, N. Prakash, Y. Hayakawa, Single-step synthesis and catalytic activity of structure-controlled nickel sulfide nanoparticles, CrystEngComm 17 (29) (2015) 5431–5439, https://doi.org/10.1039/C5CE00742A.
[48] B. Wang, J. Liu, Q. Sun, R. Li, T.-K. Sham, X. Sun, Atomic layer deposition of lithium phosphates as solid-state electrolytes for all-solid-state microbatteries, Nanotechnology 25 (50) (2014) 504007, https://doi.org/10.1088/0957-4484/25/50/504007.